Supporting Information

Bifunctional and durable $MoSe_2$-$RuSe_2$ heterojunction catalyst for alkaline seawater splitting

Shengqi Fan, Junhao Fu, Hongming Chen, Mengxiang Liu, Xueyan Zhang*, Lijie Luo* and Yongjun Chen*

School of Materials Science and Engineering, Hainan University, Haikou 570228, China.

*Corresponding authors. E-mails: zhangxy147@hainanu.edu.cn (X. Zhang), luolijie4567@163.com (L. Luo), chenyjtg@163.com (Y. Chen)

Figure captions

Figure S1 SEM images of (a) $MoSe_2$/NF and (b) $RuSe_2$/NF.

Figure S2 Nitrogen (N_2) adsorption-desorption isotherms of $MoSe_2$-$RuSe_2$ at 77 K.

Figure S3 XRD patterns of $MoSe_2$-$RuSe_2$.

Figure S4 XPS survey spectrum of $MoSe_2$-$RuSe_2$/NF.

Figure S5 High-resolution XPS spectra of Ni 2p in $MoSe_2$/NF, $RuSe_2$/NF and $MoSe_2$-$RuSe_2$/NF.

Figure S6 High-resolution XPS spectra of Se 3d in $MoSe_2$-$RuSe_2$ and $MoSe_2$-$RuSe_2$/NF.

Figure S7 CV curves of (a) NF, (b) Pt/C, (c) $MoSe_2$/NF, (d) $RuSe_2$/NF, and (e) $MoSe_2$-$RuSe_2$/NF for HER in capacitive region at scan rates from 20 to 120 mV s^{-1} in 1.0 M KOH.

Figure S8 CV curves of (a) NF, (b) RuO_2, (c) $MoSe_2$/NF, (d) $RuSe_2$/NF, and (e) $MoSe_2$-$RuSe_2$/NF for OER in capacitive region at scan rates from 20 to 120 mV s^{-1} in 1.0 M KOH.

Figure S9 Chronopotentiometry test of $MoSe_2$-$RuSe_2$/NF at 500 mA cm^{-2} for HER and OER in 1.0 M KOH.

Figure S10 CV curves of $MoSe_2$-$RuSe_2$/NF for HER in capacitive region at scan rates from 20 to 120 mV s^{-1} in (a) 1.0 M KOH, (b) 1.0 M KOH + 0.5 M NaCl and (c) 1.0 M KOH + seawater.

Figure S11 CV curves of $MoSe_2$-$RuSe_2$/NF for OER in capacitive region at scan rates from 20 to 120 mV s^{-1} in (a) 1.0 M KOH, (b) 1.0 M KOH + 0.5 M NaCl and (c) 1.0 M KOH + seawater.

Figure S12 HER and OER performances in 1.0 M KOH + seawater. (a and d) LSV curves for HER and OER, (b and e) Tafel slopes, (c) overpotential at 10, 100, 200 and 500 mA cm^{-2} and (f) Chronopotentiometry test of $MoSe_2$-$RuSe_2$/NF at 500 mA cm^{-2} for HER and OER.

Figure S13 CV curves of $MoSe_2$-$RuSe_2$/NF catalysts with Mo/Ru ratios of (a) 3:1, (b) 4:1, (c) 5:1 and (d) 6:1 for HER in capacitive region at scan rates from 20 to 120 mV s^{-1} in 1.0 M KOH + seawater.

Figure S14 Scanning rate dependence of capacitance current of $MoSe_2$-$RuSe_2$/NF catalysts with various Mo/Ru ratios for HER in capacitive region at scan rates from 20 to 120 mV s^{-1} in 1.0 M KOH + seawater.

Figure S15 CV curves $MoSe_2$-$RuSe_2$/NF catalysts with Mo/Ru ratio of (a) 3:1, (b) 4:1, (c) 5:1

and (d) 6:1 for OER in capacitive region at scan rates from 20 to 120 mV s^{-1} in 1.0 M KOH + seawater.

Figure S16 Scanning rate dependence of capacitance current of $MoSe_2$-$RuSe_2$/NF catalyst with various Mo/Ru ratios for OER in capacitive region at scan rates from 20 to 120 mV s^{-1} in 1.0 M KOH + seawater.

Figure S17 LSV curves for overall water splitting in 1.0 M KOH + seawater and seawater.

Figure S18 LSV curves of $MoSe_2$-$RuSe_2$/NF before and after stability test for (a) HER and (b) OER in 1.0 M KOH + seawater.

Figure S19 IV test of two electrodes, and the slops represent the electrical conductivity.

Figure S20 Faradaic efficiency measurements of O_2 in 1.0 M KOH + seawater. (a) Photograph of the as-constructed water electrolyzer and water drainage system with recorded scales measuring produced gases. (b) Experimental gas volumes of H_2 and O_2 during water splitting at a current density of 400 mA cm^{-2}, and the corresponding FE of $MoSe_2$-$RuSe_2$/NF.

Figure S21 SEM images of $MoSe_2$-$RuSe_2$/NF after stability test with different magnifications.

Figure S22 High-resolution XPS spectra of $MoSe_2$-$RuSe_2$/NF after stability test. (a) Mo 3d, (b) Ru 3d, (c) Ru 3p and (d) Se 3d.

Figure S23 Theoretical calculation model of (a) (015) crystal plane of $MoSe_2$, (b) (211) crystal plane of $RuSe_2$ and (c) $MoSe_2$-$RuSe_2$.

Figure S24 The adsorption model of (a) $MoSe_2$, (b) $RuSe_2$ and (c)$MoSe_2$-$RuSe_2$ for H_2O.

Figure S25 DOS of $MoSe_2$, $RuSe_2$ and $MoSe_2$-$RuSe_2$.

Figure S26 Charge density difference maps of different catalysts. (a) $MoSe_2$, (b) $RuSe_2$ and (c) $MoSe_2$-$RuSe_2$. Blue regions represent electron depletion, and yellow regions represent electron accumulation.

Table S1 The ICP of $MoSe_2$-$RuSe_2$/NF.

Table S2 Performance comparison between the $MoSe_2$-$RuSe_2$/NF based catalysts and recently reported electrocatalysts at 100 mA cm^{-2}.

Table S3 Bader charge analysis of $MoSe_2$-$RuSe_2$.

Experimental Section

1. Materials

Ruthenium (III) chloride anhydrous ($RuCl_3$, Ru content 45~55%), Sodium borohydride ($NaBH_4$, >98%), Platinum on charcoal (Pt, 20%) and Ruthenium dioxide (RuO_2, 99.9%) were purchased from Shanghai Macklin Biochemical Co. Ltd., China. Potassium hydroxide (KOH) and Sodium molybdate dihydrate ($Na_2MoO_4 \cdot 2H_2O$, 99.0%) were bought from Shanghai Aladdin Bio-Chem Technology Co. Ltd., China. Hydrochloric acid (HCl, 36%) was got from Guangdong Xi long Chemical Reagent Co. Ltd., China. Nafion perfluorinated resin solution (5 wt.%) was purchased from Sigma Aldrich. All the chemicals were used directly without further purification.

2. Characterization

The samples were characterized by field emission scanning electron microscope (FE-SEM, Hitachi S-4800, Japan), transmission electron microscope (TEM, Thermo Scientific Talos F200X) with energy dispersive X-ray spectroscopy (EDX) accessory, X-ray diffraction (XRD) with Cu Kα radiation (λ=1.5418 Å) at 2θ range of 10-90° (Bruker, AXS D8 Advance, Germany), Raman spectrometer (Renishaw In Via), X-ray photoemission spectroscopy (XPS, Thermo Scientific K-Alpha spectrometer), inductively coupled plasma optical emission spectrometer (ICP-OES, Agilent ICP OES 730). The sample digestion process for ICP-OES test was added in aqua regia solution and heated at 180 °C for 8 h. And C 1s value was set at 284.8 eV for charge corrections during XPS analysis. The specific surface areas of samples were conducted on Micromeritics ASAP 2460 system using the Brunauer-Emmett-Teller (BET) method, and N_2 adsorption/desorption property was measured at 77 K. The detection and quantification of Cl^- were carried out using an ion chromatograph (IC) (Thermo Fisher Scientific ICS-600).

3. Electrochemical measurements

The catalysts electrochemical performances of hydrogen evolution reaction (HER) and oxygen evolution reaction (OER) were tested through a three-electrode system on the electrochemical workstation (CHI 660E). The as-prepared electrodes (3 mm × 3 mm), carbon rods, and Hg/HgO served as the working electrode, counter and reference electrode, respectively. Linear sweep voltammetry (LSV) curves were conducted in 1.0 M KOH, 1.0 M

KOH + 0.5 NaCl and 1.0 M KOH + seawater solution with a scan rate of 5 mV s^{-1} at 25 ℃. For HER and OER, cyclic voltammetry (CV) measurements were conducted with various scan rates in the potential ranges of 0.8-0.9 V and 0.3-0.4 V, respectively.

To prepare Pt/C/NF or RuO_2/NF working electrodes: 2.5 mg Pt/C (or RuO_2) catalyst, 240 μL ethanol, 240 μL deionized water, and 20 μL 5 wt.% Nafion solution were ultrasonically vibrated for 30 min to form ink. 10 μL of this ink was dropped onto the pretreated NF electrode surface and dried under an infrared lamp for use.

Before the HER and OER process, the three-electrode system was injected with Ar for 30 min to maintain its stability. The frequency range of electrochemical impedance spectroscopy (EIS) measurements ranged from 10^{-2} to 10^5 Hz at the open circuit potential by applying 5 mV signal. The potential was converted to RHE through equations:

$$E_{RHE} = E_{Hg/HgO} + 0.924\,V \qquad (1)$$

The H_2 conversion efficiencies of $MoSe_2$-$RuSe_2$/NF were evaluated from the TOF values, which were obtained according to the following equation:[1]

$$TOF(s^{-1}) = \frac{jA}{2Fn} \qquad (2)$$

Where j is the current density, A is the working electrode area, 2 is the number of electrons consumed to form 1 mol H_2, F represents the Faraday constant (96500 C mol^{-1}), n (mol) is the number of moles of loaded metals that can be evaluated based on the analysis of ICP-OES measurements (The Ru contents of $MoSe_2$-$RuSe_2$/NF is 2.34 wt%).

Table S1 The ICP of $MoSe_2$-$RuSe_2$/NF.

m_0 (g)	V_0 (mL)	Test elements	C_x (mg/kg)	W (%)
0.0516	25	Ru	287.0026906	0.03
0.0516	25	Mo	1336.197453	0.13
0.0516	25	Se	127058.735	12.7
0.0516	25	Ni	815966.7087	81.6

The Faradaic efficiency (FE) was measured using a water-displacement setup in a sealed two-compartment electrolysis cell. The $MoSe_2$-$RuSe_2$/NF sample was employed as both the cathode and anode. Throughout the constant-current electrolysis at 400 mA cm^{-2}, the H_2 and O_2 gases produced were separately collected by drainage into water-filled, graduated gas burettes from their respective compartments. The recorded gas volumes were then used to calculate the FE according to the formula below:

$$n_{act} = \frac{V_P}{RT} \quad (3)$$

$$n_{theo} = \frac{It}{nF} \quad (4)$$

$$FE = \frac{n_{act}}{n_{theo}} \times 100\% \quad (5)$$

where V is the volume of collected gas (L), p is the atmospheric pressure during the experiment (Pa), T is experimental temperature (K), n is the number of electron transfers (2 for H_2, 4 for O_2), F is Faraday's constant (96485 C mol^{-1}), R is ideal gas constant (8.314 J $mol^{-1}\cdot K^{-1}$), I is current (A), and T is power on time (s).

The energy efficiency (EE) of water electrolysis, which refers to the efficiency of converting electrical energy into the chemical energy of hydrogen, is specifically calculated as follows:

$$E_0 = \frac{\Delta G^0}{nF} \quad (6)$$

$$VE = \frac{E_0}{V} \quad (7)$$

$$EE = VE \times FE \times 100\% \quad (8)$$

Where ΔG^0 is the Gibbs free energy change for the decomposition of water into H_2 and O_2 (237.22 kJ/mol), n is the number of electron transfers, F is Faraday's constant (96485 C mol^{-1}), E_0 is the reference voltage for the low heating value of hydrogen, V is the actual slot voltage (V), VE is the voltage efficiency.

4. DFT calculations

The DFT calculations were based on projector-augmented-wave (PAW) method by the Vienna Ab Initiation Simulation Package (VASP).[2] The generalized gradient approximation (GGA) of the Perdew-Burke-Ernzerh of (PBE) functional was adopted to all reaction models.[3] The force convergence standard was 0.01 eV $Å^{-1}$, and the plane wave has a cutoff energy of 450 eV.[1] The

convergence standard of electronics was 10^{-5} eV, and 5×5×1k-point was applied to all models, Grimme's DFT-D_3 method was applied to all models. The amount of charge transfer was estimated by integrating the charge density difference projected onto two-dimensional planes, following the approaches reported[4,5].

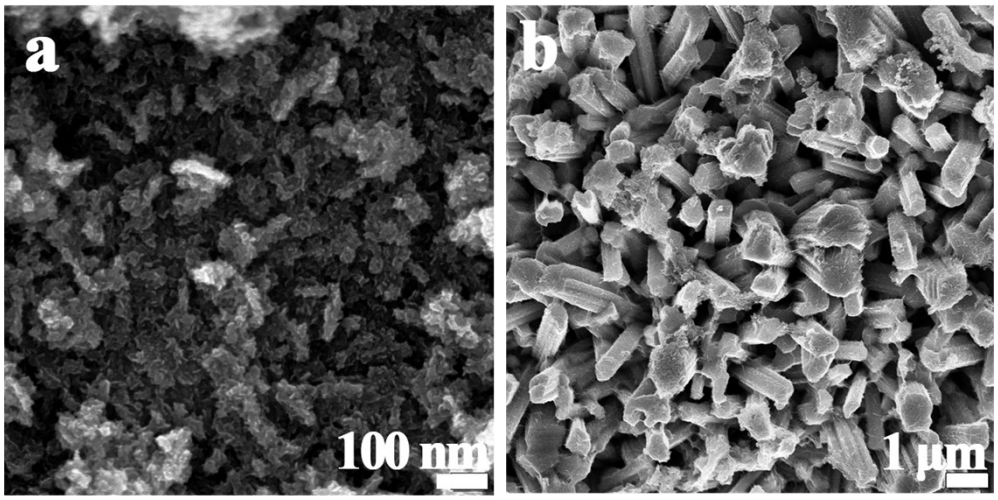

Figure S1 SEM images of (a) $MoSe_2$/NF and (b) $RuSe_2$/NF.

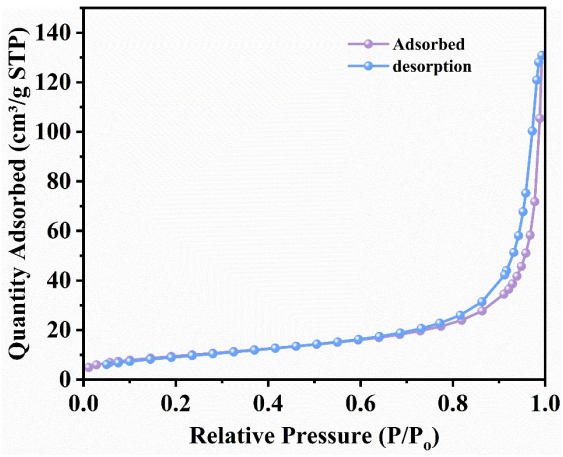

Figure S2 Nitrogen (N_2) adsorption-desorption isotherms of $MoSe_2$-$RuSe_2$ at 77 K.

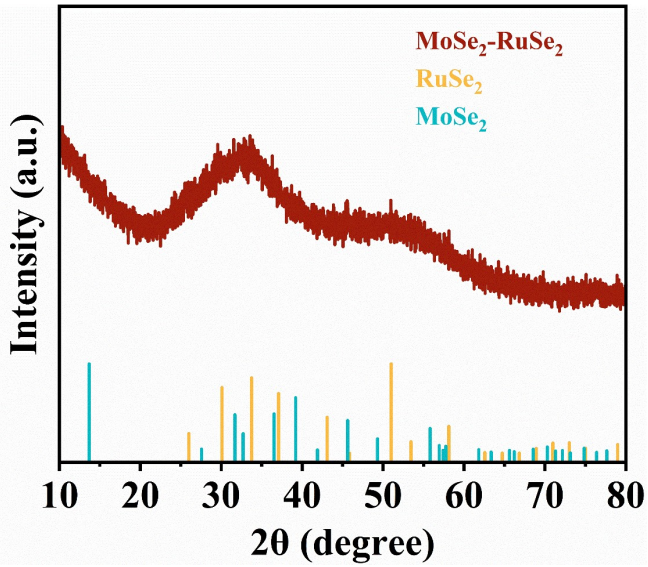

Figure S3 XRD patterns of $MoSe_2$-$RuSe_2$.

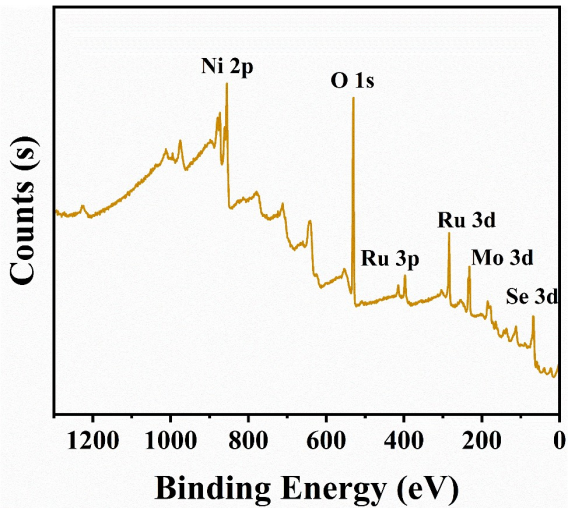

Figure S4 XPS survey spectrum of $MoSe_2$-$RuSe_2$/NF.

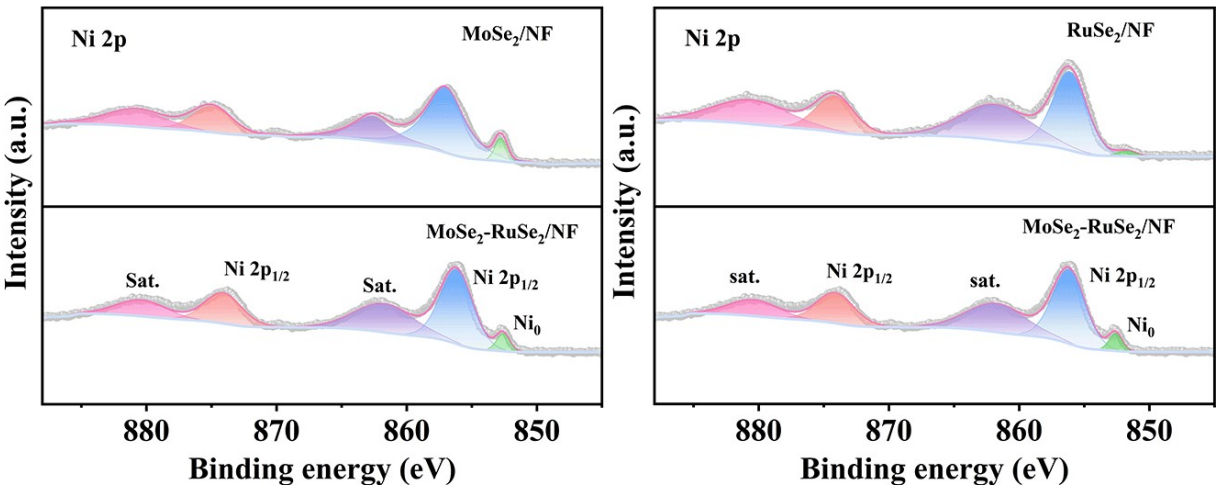

Figure S5 High-resolution XPS spectra of Ni 2p in $MoSe_2$/NF, $RuSe_2$/NF and $MoSe_2$-$RuSe_2$/NF.

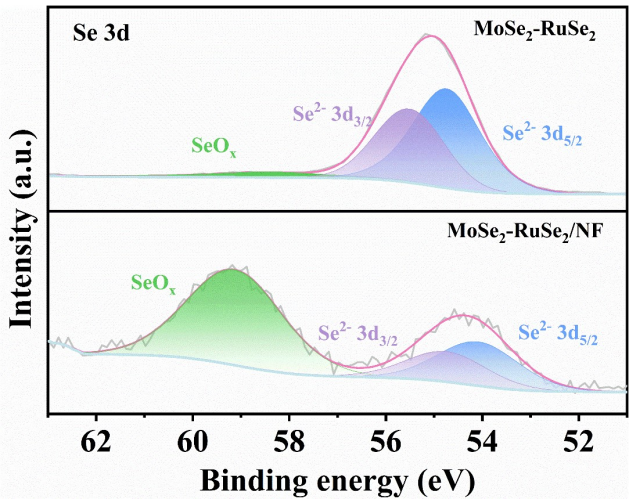

Figure S6 High-resolution XPS spectra of Se 3d in $MoSe_2$-$RuSe_2$ and $MoSe_2$-$RuSe_2$/NF.

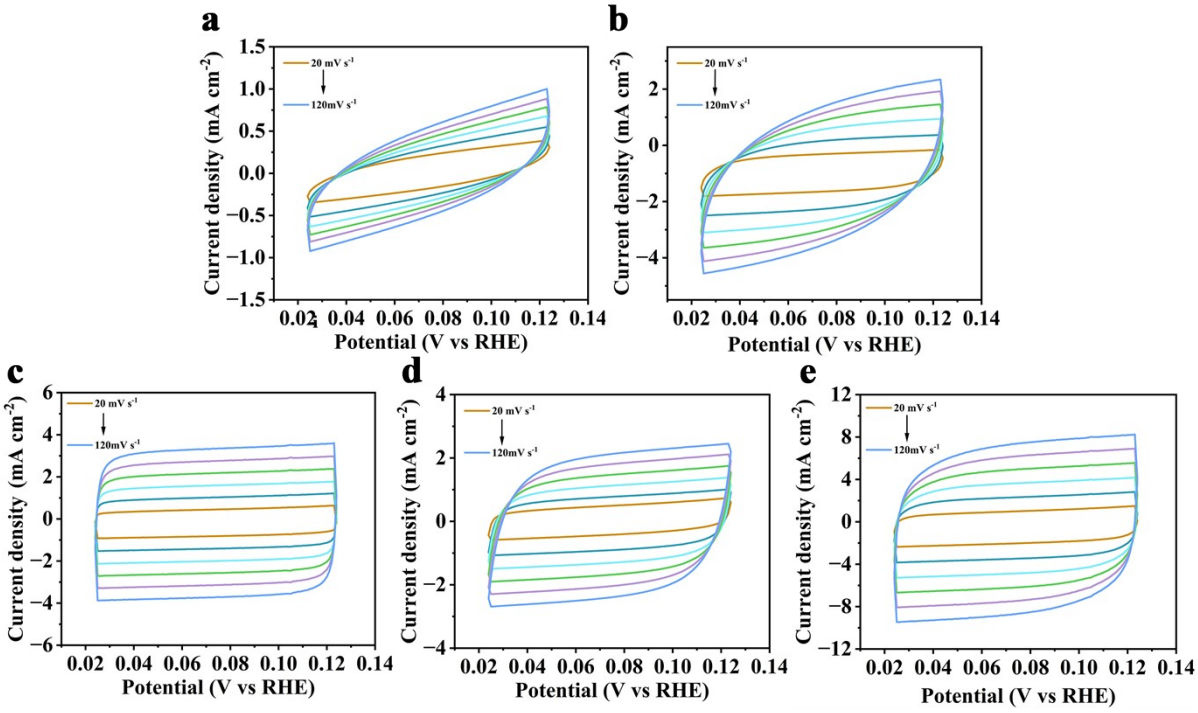

Figure S7 CV curves of (a) NF, (b) Pt/C, (c) $MoSe_2$/NF, (d) $RuSe_2$/NF, and (e) $MoSe_2$-$RuSe_2$/NF for HER in capacitive region at scan rates from 20 to 120 mV s^{-1} in 1.0 M KOH.

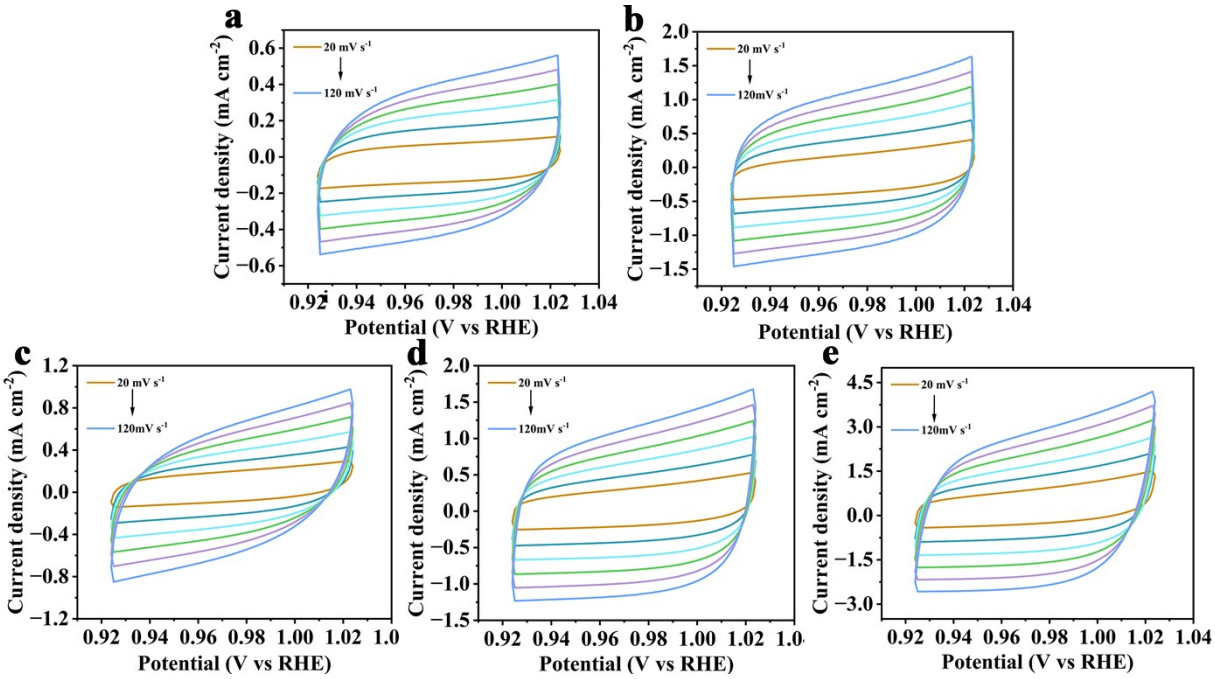

Figure S8 CV curves of (a) NF, (b) RuO_2, (c) $MoSe_2$/NF, (d) $RuSe_2$/NF, and (e) $MoSe_2$-$RuSe_2$/NF for OER in capacitive region at scan rates from 20 to 120 mV s^{-1} in 1.0 M KOH.

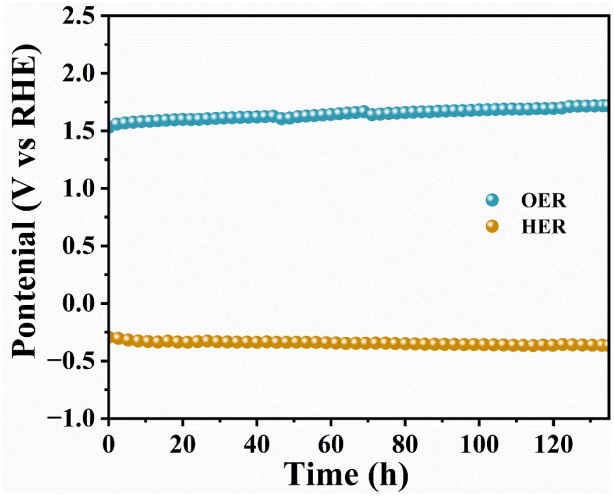

Figure S9 Chronopotentiometry test of $MoSe_2$-$RuSe_2$/NF at 500 mA cm^{-2} for HER and OER in 1.0 M KOH.

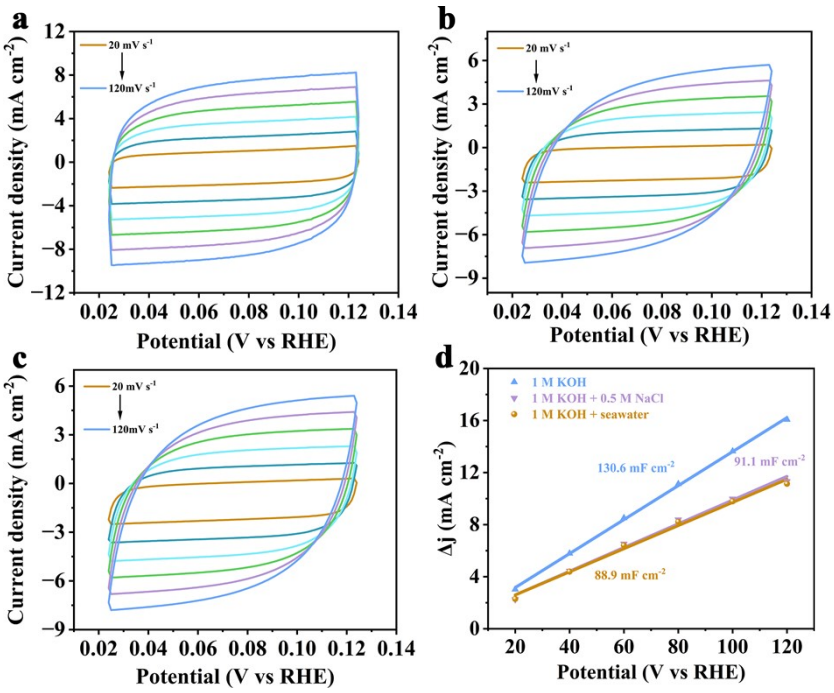

Figure S10 CV curves of $MoSe_2$-$RuSe_2$/NF for HER in capacitive region at scan rates from 20 to 120 mV s^{-1} in (a) 1.0 M KOH, (b) 1.0 M KOH + 0.5 M NaCl and (c) 1.0 M KOH + seawater.

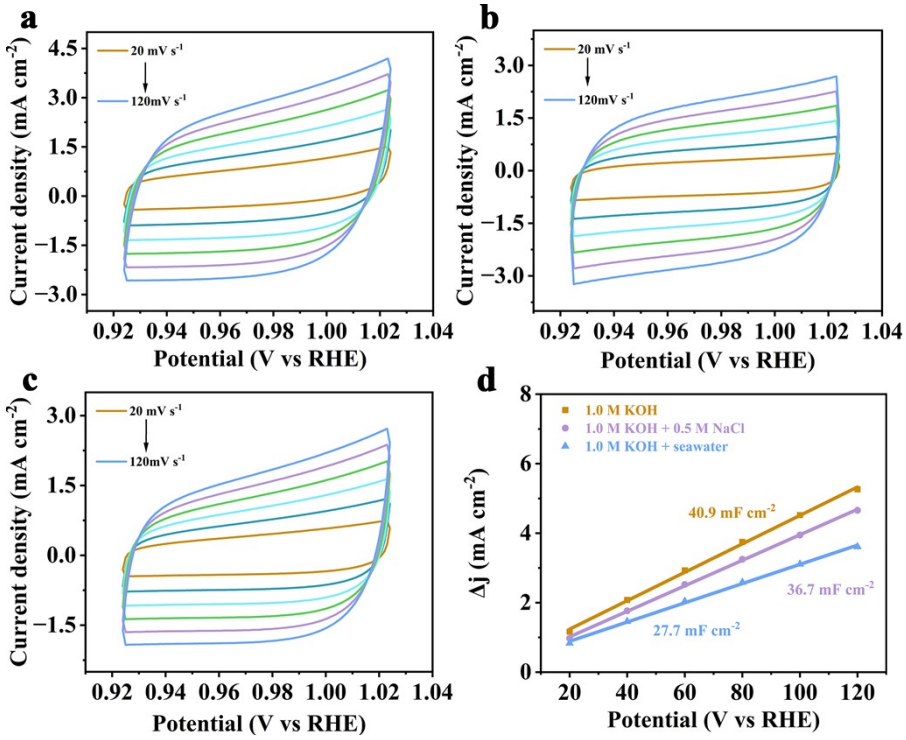

Figure S11 CV curves of $MoSe_2$-$RuSe_2$/NF for OER in capacitive region at scan rates from 20 to 120 mV s^{-1} in (a) 1.0 M KOH, (b) 1.0 M KOH + 0.5 M NaCl and (c) 1.0 M KOH + seawater.

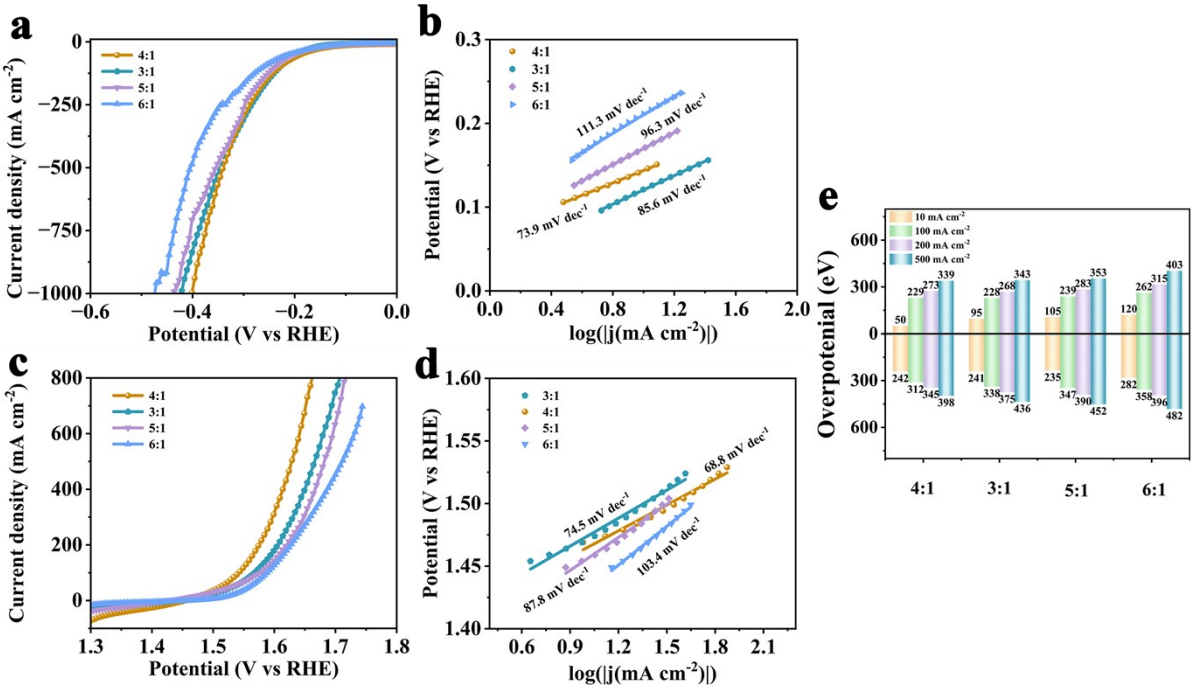

Figure S12 HER and OER performances in 1.0 M KOH + seawater. (a and d) LSV curves for HER and OER, (b and e) Tafel slopes, (c) overpotential at 10, 100, 200 and 500 mA cm^{-2} and (f) Chronopotentiometry test of $MoSe_2$-$RuSe_2$/NF at 500 mA cm^{-2} for HER and OER.

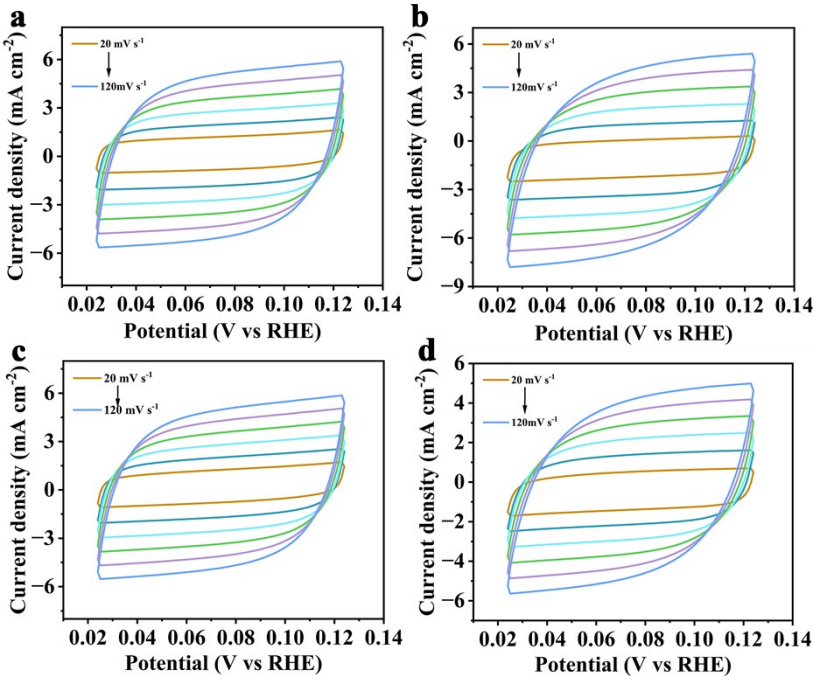

Figure S13 CV curves of $MoSe_2$-$RuSe_2$/NF catalysts with Mo/Ru ratios of (a) 3:1, (b) 4:1, (c) 5:1 and (d) 6:1 for HER in capacitive region at scan rates from 20 to 120 mV s^{-1} in 1.0 M KOH + seawater.

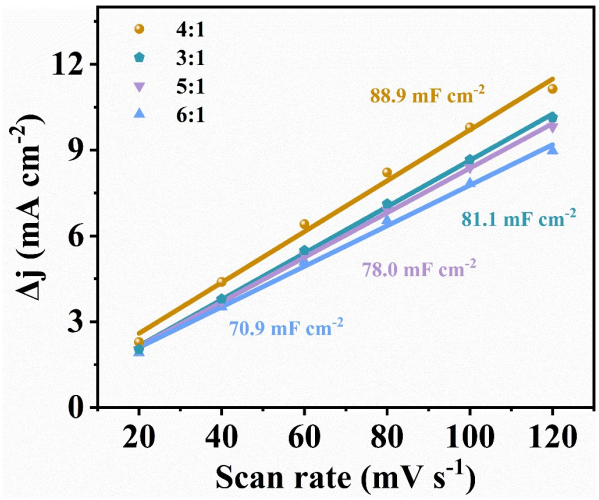

Figure S14 Scanning rate dependence of capacitance current of $MoSe_2$-$RuSe_2$/NF catalysts with various Mo/Ru ratios for HER in capacitive region at scan rates from 20 to 120 mV s^{-1} in 1.0 M KOH + seawater.

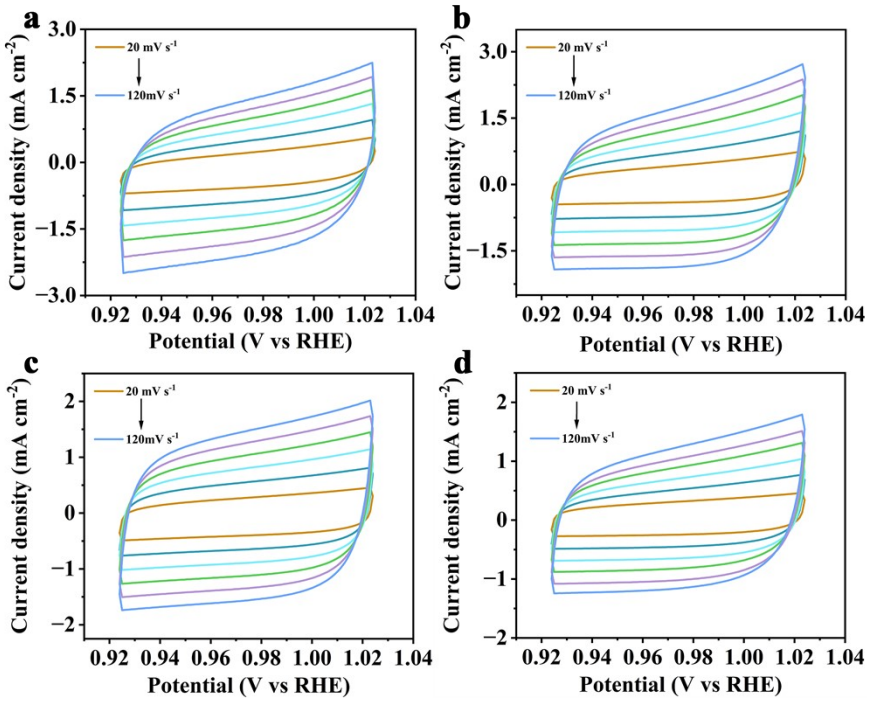

Figure S15 CV curves $MoSe_2$-$RuSe_2$/NF catalysts with Mo/Ru ratio of (a) 3:1, (b) 4:1, (c) 5:1 and (d) 6:1 for OER in capacitive region at scan rates from 20 to 120 mV s^{-1} in 1.0 M KOH + seawater.

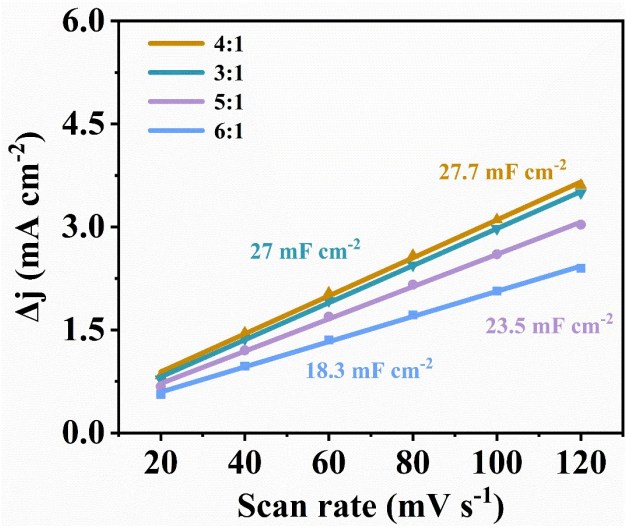

Figure S16 Scanning rate dependence of capacitance current of $MoSe_2$-$RuSe_2$/NF catalyst with various Mo/Ru ratios for OER in capacitive region at scan rates from 20 to 120 mV s^{-1} in 1.0 M KOH + seawater.

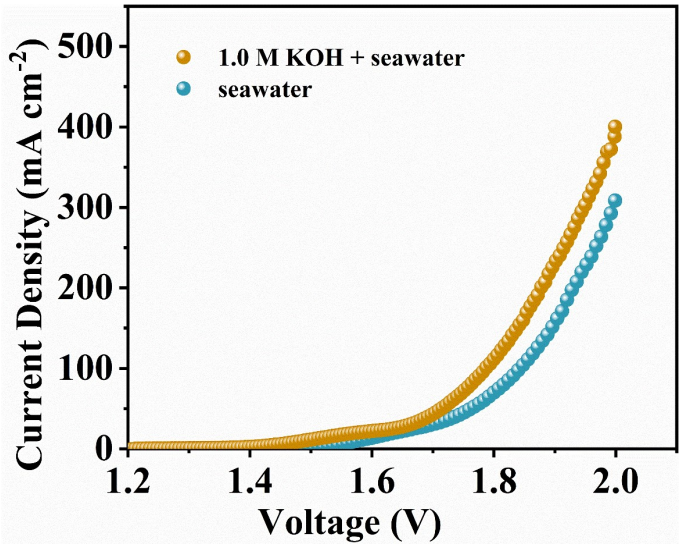

Figure S17 LSV curves for overall water splitting in 1.0 M KOH + seawater and seawater.

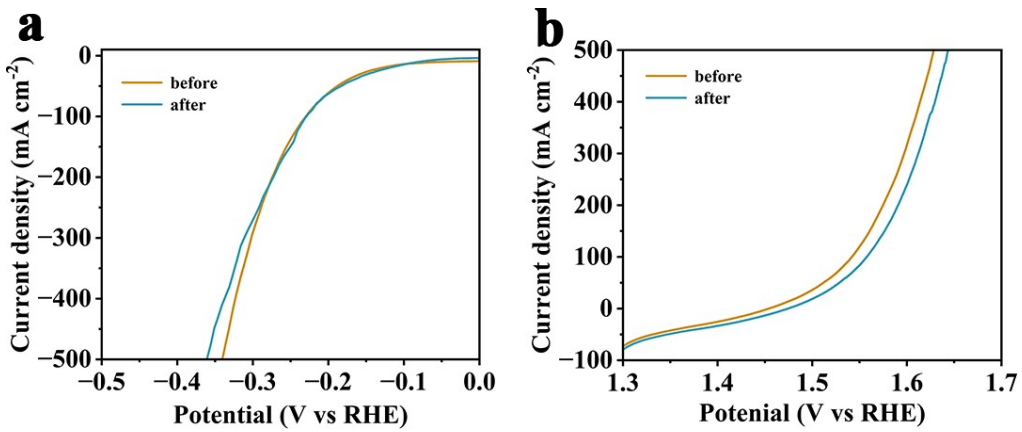

Figure S18 LSV curves of $MoSe_2$-$RuSe_2$/NF before and after stability test for (a) HER and (b) OER in 1.0 M KOH + seawater.

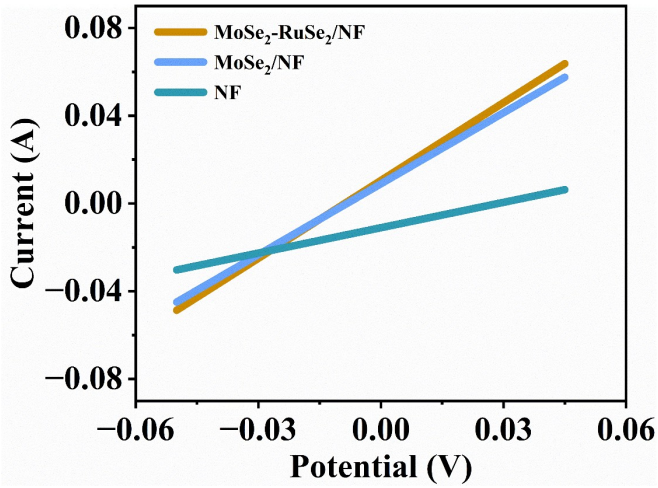

Figure S19 IV test of two electrodes, and the slops represent the electrical conductivity.

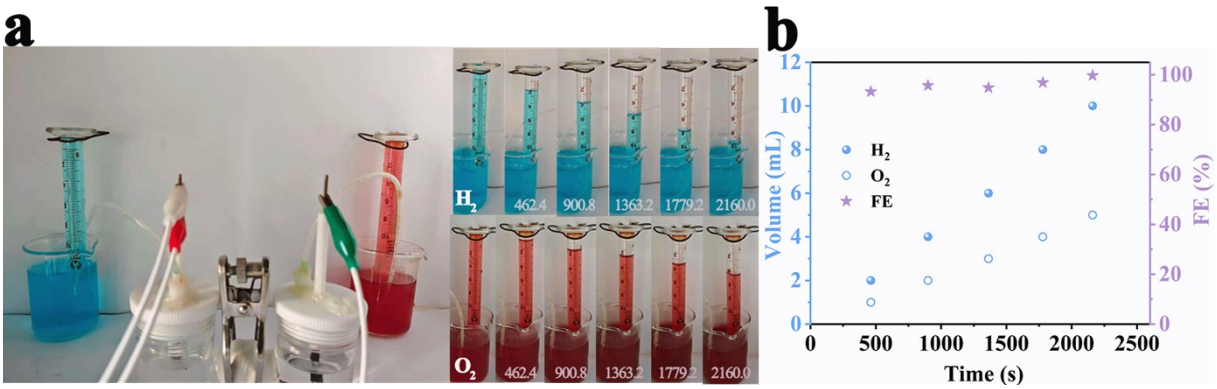

Figure S20 Faradaic efficiency measurements of O_2 in 1.0 M KOH + seawater. (a) Photograph of the as-constructed water electrolyzer and water drainage system with recorded scales measuring produced gases. (b) Experimental gas volumes of H_2 and O_2 during water splitting at a current density of 400 mA cm^{-2}, and the corresponding FE of $MoSe_2$-$RuSe_2$/NF.

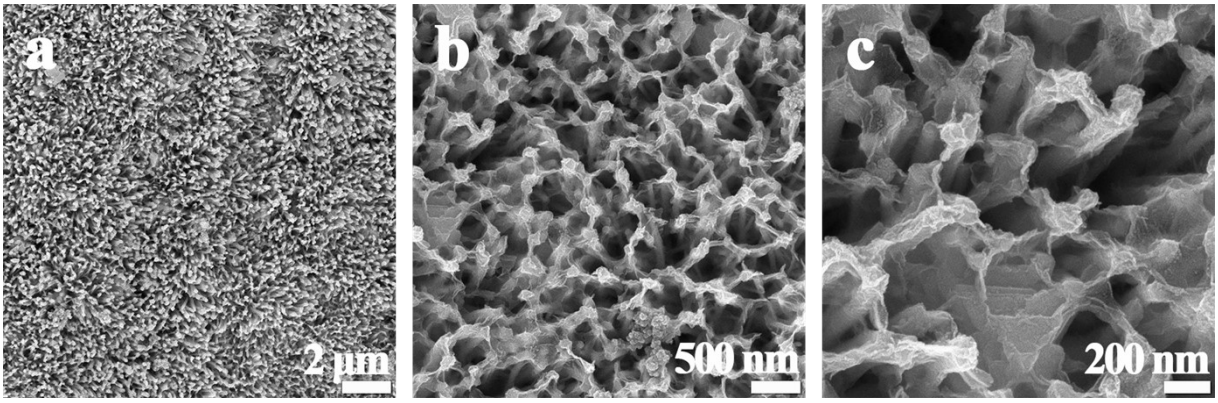

Figure S21 SEM images of $MoSe_2$-$RuSe_2$/NF after stability test with different magnifications.

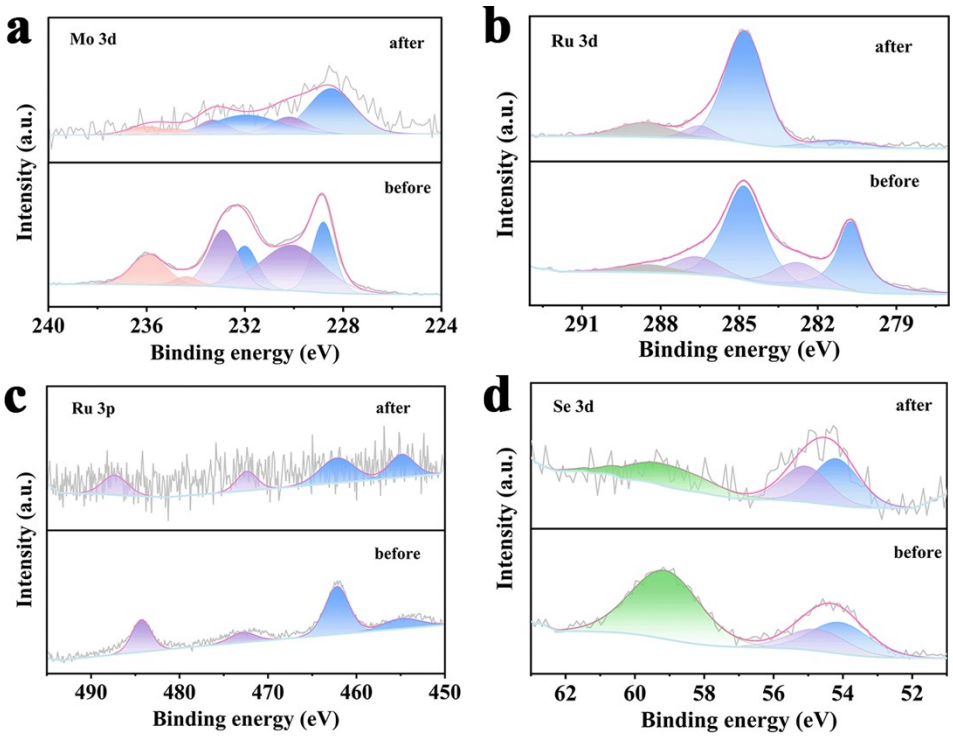

Figure S22 High-resolution XPS spectra of $MoSe_2$-$RuSe_2$/NF after stability test. (a) Mo 3d, (b) Ru 3d, (c) Ru 3p and (d) Se 3d.

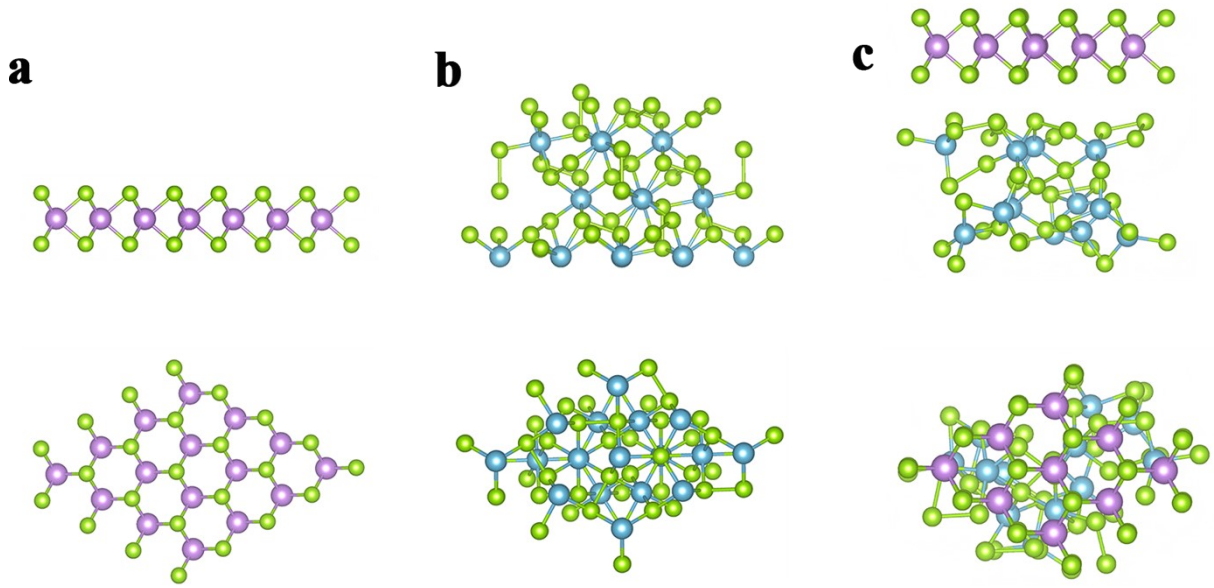

Figure S23 Theoretical calculation model of (a) (015) crystal plane of $MoSe_2$, (b) (211) crystal plane of $RuSe_2$ and (c) $MoSe_2$-$RuSe_2$.

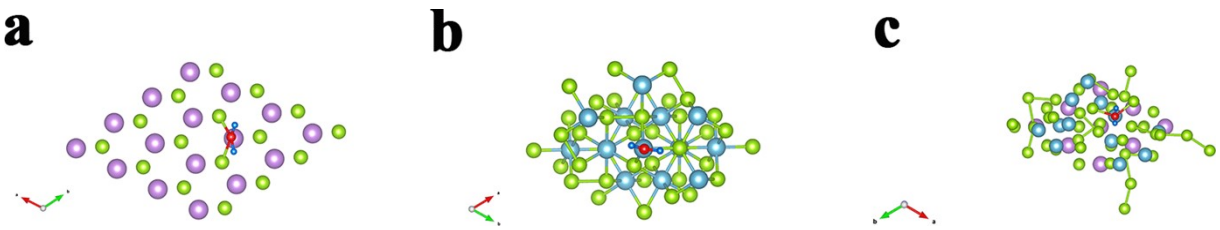

Figure S24 The adsorption model of (a) $MoSe_2$, (b) $RuSe_2$ and (c)$MoSe_2$-$RuSe_2$ for H_2O.

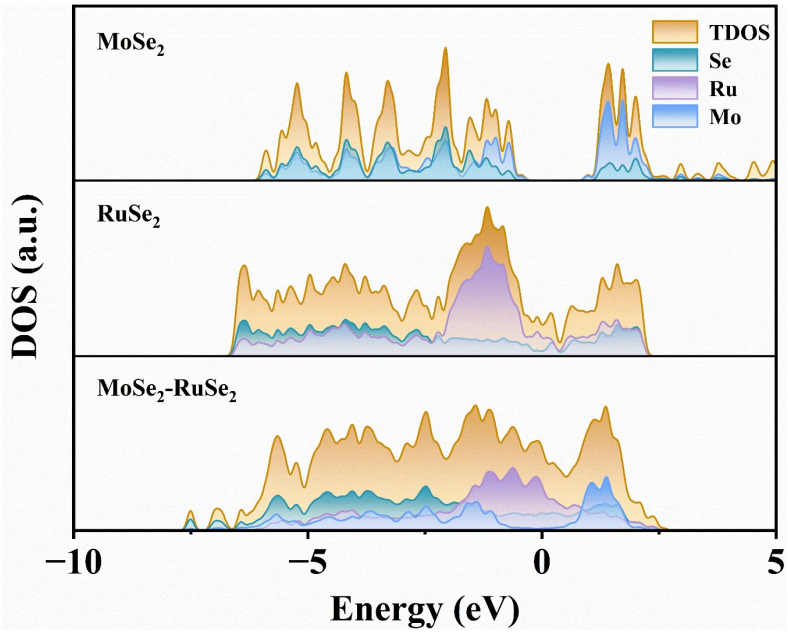

Figure S25 DOS of $MoSe_2$, $RuSe_2$ and $MoSe_2$-$RuSe_2$.

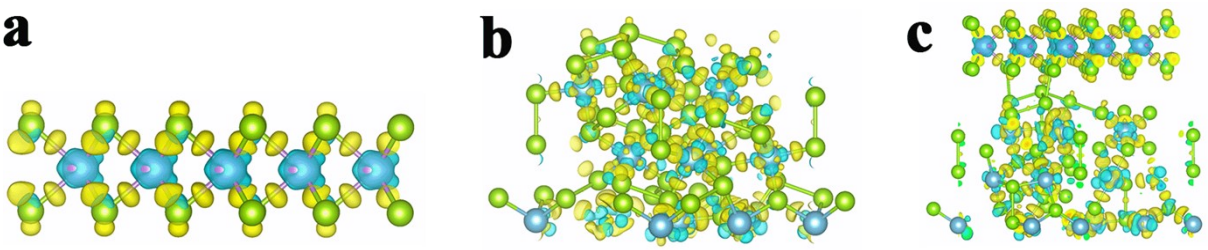

Figure S26 Charge density difference maps of different catalysts. (a) $MoSe_2$, (b) $RuSe_2$ and (c) $MoSe_2$-$RuSe_2$. Blue regions represent electron depletion, and yellow regions represent electron accumulation.

Table S2 Performance comparison between the $MoSe_2$-$RuSe_2$/NF based catalysts and recently reported electrocatalysts at 100 mA cm^{-2}.

Electrolyzer	Electrolytes	Cell Voltge (V)	Stability (h)	References
NiFeCd-LDH (+, -)	1.0 M KOH + seawater	1.79	30	6
$RuSe_2CoSe_2$/NC (+, -)	1.0 M KOH	1.77	140	7
CoS_2@CoFe-LDH (+, -)	1.0 M KOH + seawater	1.80	45	8
NiFe-LDH@NiCoP/NF (+, -)	1.0 M KOH	1.90	100	9
Ni_2P-Fe_2P/NF (+, -)	1.0 M KOH	1.68	\	10
	1.0 M KOH + seawater	1.81	48	
Co-NC/CFP (+, -)	1.0 M KOH	1.85	100	11
ZnP@Ni_2P-$NiSe_2$ (+,-)	1.0 M KOH + seawater	1.75	35	12
$Ni_{2.5}$-CuMoSe/NF (+, -)	1.0 M KOH	1.87	120	13
Ru/Ni_3NNi (+, -)	1.0 M KOH	1.76	20	14
V-Co_3O_4(Ov)-250(+, -)	1.0 M KOH + seawater	1.68	100	15
Co-Mo-50-9 h (+, -)	1.0 M KOH	1.75	96	16
NiP_2-Mo_8P_5@NF (–) || RuO_2@NF (+)	1.0 M KOH	1.67	120	17
NiMoS/NFM-LDH (+, -)	1.0 M KOH	1.89	100	18

Fe-NiS_2@$NaBH_4$ (+, -)	1.0 M KOH	1.77	360	[19]
Ru-NC-500 (–) || NiFe (+)	1.0 M KOH	1.80	100	[20]
HfO_x-in-Ir SSC/CP (–) || RuO_2/CP (+)	1.0 M KOH	2.22 at 1.0 A cm^{-2}	50 at 1.0 A cm^{-2}	[21]
$MoSe_2$-$RuSe_2$/NF (+, -)	1.0 M KOH + seawater	1.76	200	This work

Table S3 Bader charge analysis of $MoSe_2$-$RuSe_2$.

Atomic species	Atomic number	Pseudo-potential charge	Barder	Change in electric charge
Mo1	1	6	6.468939	-0.468939
Mo2	2	6	6.501891	-0.501891
Mo3	3	6	6.488284	-0.488284
Mo4	4	6	6.425326	-0.425326
Mo5	5	6	6.253012	-0.253012
Mo6	6	6	6.462148	-0.462148
Mo7	7	6	6.415516	-0.415516
Mo8	8	6	6.515525	-0.515525
Mo9	9	6	6.517894	-0.517894
Se1	10	6	5.883244	0.116756
Se2	11	6	5.745158	0.254842
Se3	12	6	5.833557	0.166443
Se4	13	6	5.866031	0.133969
Se5	14	6	5.690902	0.309098
Se6	15	6	5.92397	0.07603
Se7	16	6	5.749446	0.250554
Se8	17	6	5.878596	0.121404
Se9	18	6	5.871203	0.128797
Se10	19	6	5.760931	0.239069
Se11	20	6	5.862872	0.137128
Se12	21	6	5.811588	0.188412
Se13	22	6	5.909512	0.090488
Se14	23	6	5.764111	0.235889
Se15	24	6	5.925341	0.074659
Se16	25	6	5.752929	0.247071
Se17	26	6	5.601845	0.398155
Se18	27	6	5.86255	0.13745
Se19	28	6	5.719089	0.280911
Se20	29	6	5.845836	0.154164
Se21	30	6	5.601083	0.398917
Se22	31	6	5.767909	0.232091
Se23	32	6	5.758986	0.241014
Se24	33	6	5.539712	0.460288
Se25	34	6	5.765804	0.234196
Se26	35	6	5.911716	0.088284
Se27	36	6	5.559966	0.440034
Se28	37	6	5.71541	0.28459
Se29	38	6	5.752642	0.247358
Se30	39	6	5.565295	0.434705
Se31	40	6	5.707884	0.292116
Se32	41	6	5.779551	0.220449

Se33	42	6	5.693719	0.306281
Se34	43	6	5.708186	0.291814
Se35	44	6	5.653136	0.346864
Se36	45	6	5.68801	0.31199
Se37	46	6	5.666986	0.333014
Se38	47	6	5.759135	0.240865
Se39	48	6	5.589695	0.410305
Se40	49	6	5.583571	0.416429
Se41	50	6	5.668154	0.331846
Se42	51	6	5.645816	0.354184
Ru1	52	8	8.32154	-0.32154
Ru2	53	8	8.717556	-0.717556
Ru3	54	8	8.305555	-0.305555
Ru4	55	8	8.71485	-0.71485
Ru5	56	8	8.545444	-0.545444
Ru6	57	8	8.462906	-0.462906
Ru7	58	8	8.47978	-0.47978
Ru8	59	8	8.552004	-0.552004
Ru9	60	8	8.379533	-0.379533
Ru10	61	8	8.732465	-0.732465
Ru11	62	8	8.625287	-0.625287
Ru12	63	8	8.773466	-0.773466

References

1 Z. Chen, W. Gong, J. Wang, S. Hou, G. Yang, C. Zhu, X. Fan, Y. Li, R. Gao and Y. Cui, *Nat. Commun.*, 2023, **14**, 5363.

2 G. Kresse and J. Furthmüller, *Comput. Mater. Sci.*, 1996, **6**, 15–50.

3 J. P. Perdew, K. Burke and M. Ernzerhof, *Phys. Rev. Lett.*, 1996, **77**, 3865–3868.

4 C. Li, S. Mujtaba, J. Quan, L. Xu, X. Ning, P. Chen, Z. An and X. Chen, *Adv. Funct. Mater.*, 2025, **35**, 2501262.

5 W. Lou, G. Liu, X. Ma, C. Yang, L. Feng, Y. Liu and X. Gao, *J. Mater. Chem. A*, 2025, **13**, 4356–4366.

6 Q. Liu, K. Chen, M. Wang, H. Fan, Z. Yan, X. Du and Y. Chen, *J. Colloid Interface Sci.*, 2024, **663**, 624–631.

7 L. Li, J. Qu, L. Zhang, L. Wei, J. Su and L. Guo, *ACS Appl. Mater. Interfaces*, 2024, **16**, 24660–24670.

8 G. Afshan, S. Karim, Y. P. Kharwar, T. Aziz, S. Saha, S. Roy and A. Dutta, *Small*, 2025, **21**, 2406431.

9 H. Zhang, X. Li, A. Hähnel, V. Naumann, C. Lin, S. Azimi, S. L. Schweizer, A. W. Maijenburg and R. B. Wehrspohn, *Adv. Funct. Mater.*, 2018, **28**, 1706847.

10 L. Wu, L. Yu, F. Zhang, B. McElhenny, D. Luo, A. Karim, S. Chen and Z. Ren, *Adv. Funct. Mater.*, 2021, **31**, 2006484.

11 H. Huang, S. Zhou, C. Yu, H. Huang, J. Zhao, L. Dai and J. Qiu, *Energy Environ. Sci.*, 2020, **13**, 545–553.

12 K. Chang, D. T. Tran, J. Wang, S. Prabhakaran, D. H. Kim, N. H. Kim and J. H. Lee, *Adv. Funct. Mater.*, 2022, **32**, 2113224.

13 Y. Ha, T. Zhou, Z. Xu, X. Zhu, X. Chen, Z. Wang and Y. Liu, *Inorg. Chem.*, 2024, acs.inorgchem.4c04302.

14 Z. Liu, M. Zha, Q. Wang, G. Hu and L. Feng, *Chem. Commun.*, 2020, **56**, 2352–2355.

15 W.-J. Xu, S. U. Rahman, Y.-Y. Wang, J.-Y. Dang, X.-Y. Zhang, W.-L. Li and J. Zhang, *J. Colloid Interface Sci.*, 2025, **690**, 137354.

16 X. Zhang, A. Wu, D. Wang, Y. Xie, A. I. Gubanov, G. A. Kostin and C. Tian, *Small*, 2025, 2409703.

17 M. Gao, W. Pan, Z. Huang, L. Wang, J. Guo, S. Muhammad, C. Ruan, T. T. Isimjan and X. Yang, *J. Colloid Interface Sci.*, 2025, **683**, 1087–1095.

18 L. Mu, J. Ying, Y. Ou, Z. Wang, Y. Liu, N. Zhao, M. Xue, Y. Dai and G. Zhao, *J. Colloid Interface Sci.*, 2025, **688**, 106–117.

19 G. Xiong, H. Deng, Y. Chen, Q. Wu, X. Zhou and W. Yao, *ACS Catal.*, 2025, **15**, 13948–13957.

20 R. Boppella, P. M. Austeria, G. H. Gu and T. K. Kim, *ACS Catal.*, 2025, **15**, 16981–16991.

21 W. Shao, Z. Xing, M. Zhou, R. Yan, T. Ma, B. Yin, Y. Wang, C. Cheng, S. Li and C. Zhao, *Adv. Mater.*, 2025, **37**, 2507080.